Food Chemistry: Molecular Sciences 4 (2022) 100103

Contents lists available at ScienceDirect

Food Chemistry: Molecular Sciences

journal homepage: www.sciencedirect.com/journal/food-chemistry-molecular-sciences

DFT-based Raman spectral study of astaxanthin geometrical isomers

Guohua Yao [a,b], Muhammad Muhammad [a], Jiajiang Zhao [a], Jianguo Liu [c], Qing Huang [a,*]

[a] CAS Key Laboratory of High Magnetic Field and Ion Beam Physical Biology, Hefei Institute of Intelligent Agricuture, Institute of Intelligent Machines, Hefei Institutes of Physical Science, Chinese Academy of Sciences, Hefei 230031, China

[b] Key Laboratory of Resource Chemistry of Ministry of Education, Shanghai Key Laboratory of Rare Earth Functional Materials, Department of Chemistry, Shanghai Normal University, Shanghai 200234, China

[c] CAS and Shandong Province Key Laboratory of Experimental Marine Biology, Center for Ocean Mega-Science, Institute of Oceanology, Chinese Academy of Sciences, Qingdao 266071, China

ARTICLE INFO

Keywords:
Astaxanthin
Raman spectroscopy
Density functional theory (DFT)
Geometric isomers
Vibrational mode
Molecular science

ABSTRACT

Astaxanthin is a carotenoid widely used in food additives, nutritional product and medicines, which shows many physiological functions such as antioxidant, anti-inflammatory, anti-hypertensive and anti-diabetic activities. It has been recognized that astaxanthin has all-*trans* and nine *cis* isomers, and these geometrical isomers have very different biological activities. The process of selective enrichment, metabolism and isomerization of astaxanthin in animals remains to be studied. Therefore, identifying isomers and obtaining their structural parameters are important for understanding the active mechanism of different molecular isomers. Although the traditional methods such as high-performance liquid chromatography (HPLC) and nuclear magnetic resonance (NMR) spectroscopy can be used to distinguish these isomers, these methods generally require considerable testing time, cost, sample volume, and hardly be applied in vivo. In this work, Raman spectroscopy combined with density functional theory (DFT) calculation was introduced to study different geometrical isomers of astaxanthin. The theoretical and experimental Raman spectra are in agreement, and we have demonstrated that all the known ten geometrical isomers of astaxanthin can be readily distinguished using this spectroscopic approach. The astaxanthin molecular vibrational modes, geometric structures, energies of ten geometric isomers are systematically scrutinized. Moreover, a lot of structural and Raman problems unsolved previously have been solved by the DFT-based spectral analysis. Therefore, this work provides an effective way for identification of different astaxanthin geometrical isomers, and may have important significance for promoting the research of astaxanthin isomers on biological property mechanisms and related applications in food molecular science.

1. Introduction

Astaxanthin (AST) is a carotenoid widely distributed in nature, found in salmon, shrimp, crab and alga. AST is known as a super antioxidant, which can effectively remove free radicals from the body, and promote a variety of physiological functions, such as suppressing oxidation, lowering lipid and enhancing immunity activities (Liu and Huang, 2016; Visioli and Artaria, 2017). Therefore, it has recently attracted a lot of attention in both scientific research and applied areas (Ambati et al., 2014; de Bruijn et al., 2016; Honda et al., 2021a; Honda et al., 2021b; Liu et al., 2016; Visioli and Artaria, 2017; Yang et al., 2021; Yu and Liu, 2020). Currently, AST products have been commercially used in safe food additives, nutritional products, cosmetics, aquaculture (Ambati et al., 2014; Yang et al., 2021). The main source of human commercial food AST is extracted from algae and aquatic crustaceans.

Due to its structural characteristics, AST has many different geometric isomers. AST consists of two oxidized ionone rings connected by a long conjugated double bond system (Visioli and Artaria, 2017). The existence of many conjugated double bonds in the polyene chain makes AST have different *cis-trans* isomers, such as the all-*trans* isomer, 9-*cis*, 13-*cis* and 15-*cis* isomers, and di-*cis* isomers as well (Euglert and Vecchi, 1980; Holtin et al., 2009). In fact, there are ten known *cis-trans* geometrical isomers, namely, the all-*trans* isomer, three mono-*cis* forms (e.g., 9-*cis*, 13-*cis*, 15-*cis* isomers), and six kinds of di-*cis* isomers (e.g., 9,9′-di-*cis*, 9,13-di-*cis*, 9, 13′-di-*cis*, 9,15-di-*cis*, 13,13′-di-*cis*, 13, 15-di-*cis* isomers) (Euglert and Vecchi, 1980). The all-*trans* isomer and the *cis* isomers may convert to each other under certain conditions, such as high temperature, exposure to light, the presence of acid, organic or metal ion

* Corresponding author.
E-mail address: huangq@ipp.ac.cn (Q. Huang).

https://doi.org/10.1016/j.fochms.2022.100103
Received 28 November 2021; Received in revised form 9 March 2022; Accepted 12 March 2022
Available online 14 March 2022

solvents (Euglert and Vecchi, 1980; Liu and Osawa, 2007; Osterlie et al., 1999; Yuan and Chen, 1999; Zhao et al., 2005). Spectral and theoretical studies of carotenoids have also revealed that the presence of the additional dark singlet excited states and the protein surrounding environment would cause the geometrical deformations of carotenoids (Macernis et al., 2012).

Since AST has been widely studied and applied, it is important to study whether there are specific functional differences between AST isomers (Yu and Liu, 2020). It is now recognized that the geometrical configuration of AST isomers is closely related to the functional performance and biological activity of AST (Gong et al., 2020; Su et al., 2020; Visioli and Artaria, 2017; Yu et al., 2021; Yu and Liu, 2020). For example, during in vitro digestion, the 13-*cis* shows higher bioavailability than 9-*cis* and all-*trans* ASTs, and 9-*cis* shows higher transport efficiency than all-*trans* and 13-*cis* (Visioli and Artaria, 2017; Yang et al., 2017). Based on AST fed to male rats, it was supported that the *cis*-AST isomers, the 13-*cis* have greater bioavailability and tissue accumulation efficiency than the all-*trans*-isomer (Honda et al., 2021b). The *cis* isomers of AST show much higher antioxidant efficacy than all-*trans* isomer in vitro (Liu and Osawa, 2007). The *cis*-AST, especially 9-*cis* AST exhibits greater anti-inflammatory effect than all-*trans* isomer (Yang et al., 2019). The 9-*cis* and 13-*cis* ASTs show a higher protection against oxidative stress than all-*trans* AST against oxidative stress (Yang et al., 2017). The 9-*cis* has higher storage stability than the other *cis*-isomers in oils and fats, because during storage, the 13-*cis* and 15-*cis* isomers will be isomerized into all-*trans* isomer during the storage but 9-*cis* AST is barely isomerized (Honda et al., 2021a). It is known that isomers of other carotenoids also exhibit different biological properties. For example, it is reported that the mono-*cis* configuration (15-*cis*) of neurosporene is bound to the reaction center, while the all-*trans*-neurosporene is bound to the light-harvesting complex (Koyama et al., 1988; Koyama et al., 1982).

In this regard, therefore, more in-depth and detailed research is required to verify the existence of isomerization and distinguish the structural differences of the isomers. Previous studies used analytical methods such as Nuclear Magnetic Resonance (NMR) and High Performance Liquid Chromatography (HPLC) to detect and study geometry isomers of AST (Buchwald and Jencks, 1968; Euglert and Vecchi, 1980; Holtin et al., 2009; Osterlie et al., 1999; Zajac et al., 2018). For example, High-performance liquid chromatography-mass spectrometry (HPLC-MS) and NMR spectroscopy were applied to separate the components of the complex AST and distinguish the all-*trans*, 9-*cis* and 13-*cis* isomers (Holtin et al., 2009; Osterlie et al., 1999). X-ray diffraction was used to resolve crystal structures of unbound, chloroform solvate, pyridine solvate of all-*trans* AST (Bartalucci et al., 2007). However, these techniques usually require considerable time, sample volume and cost for the inspection and analysis. More importantly, these tools can hardly be applied to the in vivo identification of AST isomers in living cells. For example, to clarify the bioavailability and tissue accumulation efficiency of AST isomers, current researchers could only evaluate the AST isomer contents by HPLC in vitro after the tested rats were killed (Honda et al., 2021b).

If different astaxanthin isomers can be traced in a living body, it is certain that the properties and biological significance of the different isomers can be studied more deeply, so as to expand the application of AST in food science, nutrition, medical, aquatic feed, etc. In recent years, Raman spectroscopy as in vitro and in vivo detection technology, has also been introduced to detect and study AST, mainly all-*trans* isomer (Huang et al., 2010; Kaczor et al., 2011; Liu and Huang, 2016; Shao et al., 2019; Sharma et al., 2015; Subramanian et al., 2014). However, there are still many problems to be solved in the structure and Raman analysis of AST, which restrict the better application of Raman spectroscopy on AST. Since AST is also a type of carotenoids, there are many similarities in the vibrational spectra of AST and other carotenoids (such as typical beta-carotene). The Raman spectrum of β-carotene exhibits the main vibrational bands at about 1512, 1156, 1006 and 955 cm^{-1} which represent the ν_1 -C═C-, ν_2 -C—C-, ν_3 –CH- rocking vibrations of $–CH_3$ groups attached to the polyene chain coupled with -C—C- bonds and ν_4 -C—H out-of-plane wagging vibrations, respectively (Macernis et al., 2021; Saito and Tasumi, 1983; Streckaite et al., 2020). When the structure of the functional group changes, the corresponding characteristic bands will also change. For instance, the different Raman ν_1 band shifts were found in the β-carotene conformers with the different β-ring dihedral angles and conjugated chain lengths (Macernis et al., 2021; Macernis et al., 2014; Streckaite et al., 2020). It is clear that the vibrational spectral signals are very sensitive to the molecular structure. The AST molecule and β-carotene have the same conjugated polyene chain but different substitution pattern in the ionone ring, since AST has an hydroxyl group (OH) at the C3 site and a carbonyl group (C═O) at the C4 site. Moreover, the AST has extended conjugation into the carbonyl group of ending ring. Therefore, AST and β-carotene should have many different features on the vibrational modes and spectral signatures (Requena et al., 2008; Saito and Tasumi, 1983; Subramanian et al., 2014). However, to the best of our knowledge, there was no systematic quantum chemistry theoretical work to study Raman spectra and vibrational modes of the *cis-trans* isomers of AST. In the previous studies, when people analyzed the experimental Raman spectrum of AST, they often referred to the vibrational mode assignments of β-carotene, which could lead to some inappropriate structural and spectral analysis (Requena et al., 2008; Subramanian et al., 2014). It was reported that only six astaxanthin isomers could be distinguished from Raman spectroscopy, but ten geometric isomers have been reported (Subramanian et al., 2014). As the intensities of Raman bands of astaxanthin are extremely strong, whether this is caused by resonance Raman is also controversial (Bergamonti et al., 2011; Meinhardt-Wollweber et al., 2018; Subramanian et al., 2014). For the same Raman peak, different isomers sometimes have significantly different linewidths, which has not been reasonably explained. The reason why different isomers have different proportions in organisms has not been explained, either. For instance, all-trans configuration is roughly approximated as 70%, 9-cis and 13-cis are about 10%, the other isomers are less than 2% (Yu and Liu, 2020). The experimental crystal structure of all-trans isomer of AST was obtained through X-ray diffraction (Bartalucci et al., 2007). However, the geometric structure parameters of the *cis*-isomer of astaxanthin have not been reported. It is noteworthy that Raman spectroscopy technique has now been used for the detection of all-*trans* astaxanthin in living cells (Kaczor and Baranska, 2011). If the spectral problems could be solved, people may be able to achieve the identification and imaging of all geometric isomers of AST in living organisms, such as cells, living tissues, algae.

Therefore, to address the above questions, this present work aimed to identify all-known geometrical isomers of AST and solve the problems in structure and Raman spectroscopy. For this purpose, we employed quantum chemistry methods and Raman spectra to systematically study the structural and spectral properties of AST isomers. The structures and Raman spectra of all geometric isomers of astaxanthin were therefore systematically explored and interpreted.

2. Materials and methods

The all-*trans* isomer of AST was purchased from Aladdin Bio-Chem Technology Co., LTD, Shanghai, China. The 9-*cis* and 13-*cis* isomers of AST were purchased from ZZBIO Co., LTD, Shanghai, China.

For the Raman spectroscopy measurement, the samples were placed on a quartz plate to collect the Raman spectra, and the Stokes Raman lines were recorded in the region of 200–3700 cm^{-1} using XploRA Raman spectrometer (HORIBA JOBIN YVON, Paris, France) with a 785 nm laser. The laser power on the sample was approximately 1.2 mW, and exposure time was 5 s. The spectra were measured at least three times.

For the computation of the Raman spectra of AST isomers, density functional theory (DFT) was employed using Gaussian 09 packages

(Frisch et al., 2009). All calculations were performed by applying the B3LYP functionals, with the hybrid of Becke's nonlocal three parameter exchange functional and the Lee-Yang-Parr correlation functional. The triple-zeta 6–311 + G(d,p) split valence-shell basis set was used, which was augmented by d polarization functions on heavy atoms and p polarization functions on hydrogen atoms as well as diffuse functions for heavy atoms (Perdew et al., 1996). The geometries were optimized without any constraint and the optimized geometries do not have imaginary frequencies. Then the Raman spectra were simulated with a resolution of 8 cm^{-1} at the same theories. The vibrational frequency scaling factor for B3LYP/6–311 + G (d,p) is 0.9808 (Laury et al., 2012). The calculated Raman activities were converted into Raman intensities by using the following relation derived from the basic theory of Raman scattering:$I_i = f(\nu_0 - \nu_i)^4 A_i/\nu_i[1 - exp(-hc\nu_i/kT)]$, where ν_0 is the exciting frequency (in cm^{-1}), ν_i is the vibrational frequency (in cm^{-1}) of the *i*th normal mode, *h*, *c*, and *k* are fundamental constants, and *f* is a common normalization factor for all band intensities. The assignments of vibrational models and their potential energy distributions (PEDs) were obtained using the Gaussview 5.0.8 program and VEDA 4xx program (Dennington et al., 2009; Jamróz, 2013).

The initial geometry structure of all-*trans* AST was derived from the crystal structure data of unbound all-*trans* AST which is the mixture of 3*S*,3′*S*: 3*R*,3′*S*: 3*R*,3′*R* in a 1:2:1 ratio (Bartalucci et al., 2007). By statistical probability when two chiral hydroxy group are added to the same molecule the result is 1:2:1 for the *SS*, *RS* and *RR* isomers. This AXT sample consists of the *R* and *S* form ionone ring in equal amounts. Therefore, the chirality of crystal structure data is represented by 3*R*,3′*S* (Bartalucci et al., 2007). In the structural optimization calculation of this work, the calculated structures are all with 3*R*,3′*S* chirality, and the initial input structure of all-*trans* AST is from the crystal data (Bartalucci et al., 2007). The experimental crystal structure data of other geometry isomers of AST was not found. Therefore, the initial input structures of

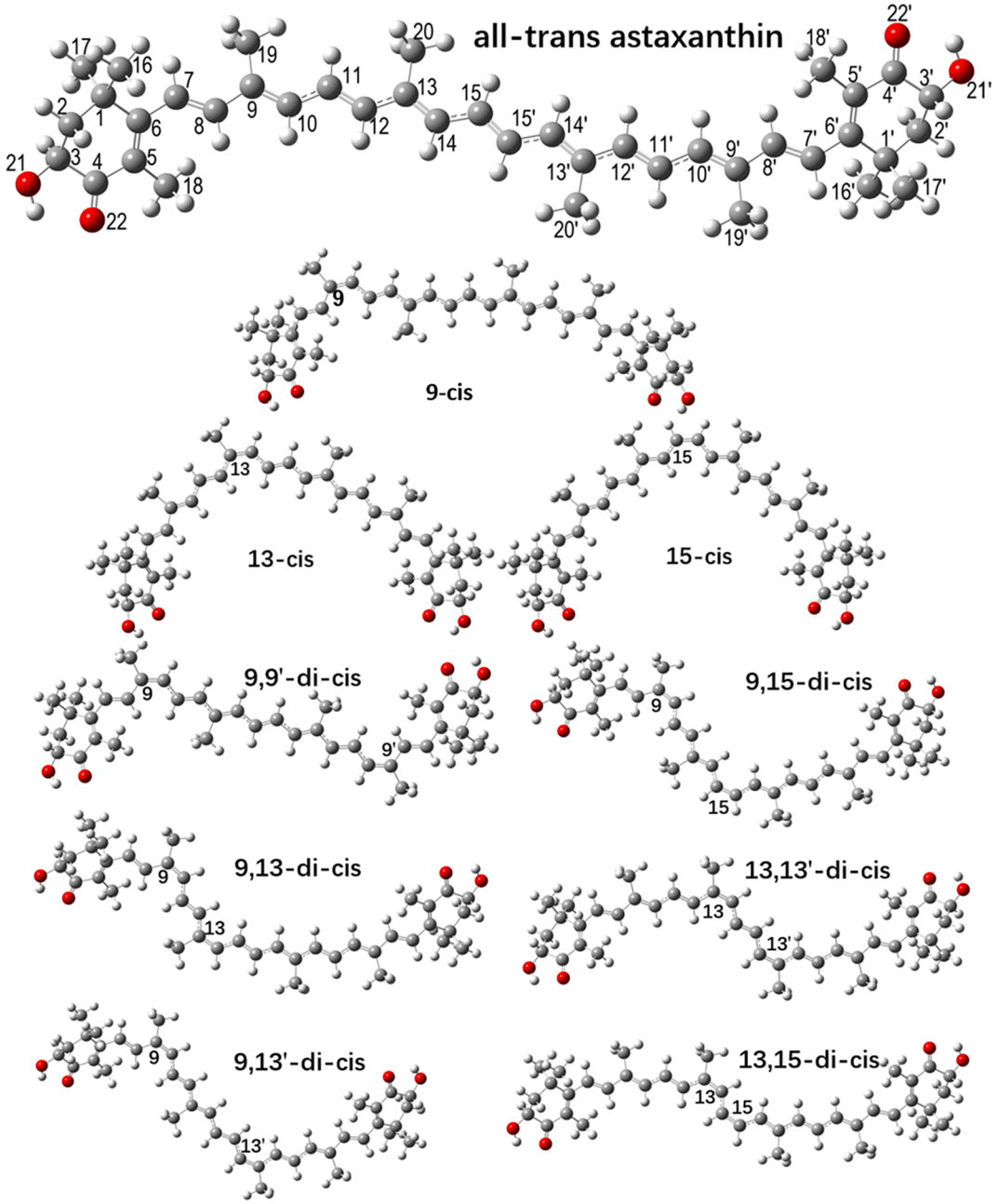

Fig. 1. The optimized geometry structure and atom labeling of all-*trans*, three mono-*cis* isomers and six di-*cis* isomers of astaxanthin molecules.

the *cis* ASTs in geometry optimizations are constructed based on the crystal data of all-*trans* AST.

Astaxanthin (3,3′-dihydroxy-β,β′-carotene-4,4′-dione, $C_{40}H_{52}O_4$) consists of a nonpolar central conjugated polyene chain and two polar cyclized end groups (hydroxyl and keto groups). The existence of multiple carbon-carbon double bonds makes AST have multiple *cis-trans* isomers. As shown in Fig. 1, all-*trans*- AST can be isomerized in to mono-*cis* forms, such as 9-*cis*, 13-*cis*, 15-*cis*, and 6 kinds of di-*cis* isomers, including 9,9′-di-*cis*, 9,13-di-*cis*, 9, 13′-di-*cis*, 9,15-di-*cis*, 13,13′-di-*cis*, 13, 15-di-*cis* which were found in plants and animals (Euglert and Vecchi, 1980; Yu and Liu, 2020). The optimized molecular structures of 10 known AST isomers are illustrated in Fig. 1. The calculated structure parameters of all-*trans* AST are compared with the experiment (Bartalucci et al., 2007), involving the bond, lengths and dihedral angles in Table S1. From Table S1, it is clear that the experimental and theoretical calculated structural parameters are very close, and the RMSD value is extremely small. The RMSD value of the calculated bond lengths with respect to experiment is only 0.016 Å. The RMSD values of the calculated angles and dihedral angles with respect to experiment are only 1.1° and 4.4°, respectively. This also means that this level of theoretical calculation is suitable for the structural simulation of AST, and the calculated structural parameters of other nine isomers may also be very valuable.

3. Results and discussion

3.1. Interpretation of Raman spectra of the geometric isomers

3.1.1. Interpretation of Raman spectrum of all-trans isomer

Since the proportions of all-*trans*, 9-*cis* and 13-*cis* AST isomers are usually more than 5% (Yu and Liu, 2020), the functional performance and biological activity of these isomers are more broadly studied (Honda et al., 2021b; Visioli and Artaria, 2017; Yang et al., 2017). The standard all-*trans*, 9-*cis* and 13-*cis* AST are commercially available. The experimental Raman spectra were measured using 785 nm laser, which are shown in Fig. 2. Similar to the Raman spectrum of β-carotene, the main Raman bands of AST at about 1520 cm^{-1}, 1160 cm^{-1} and 1006 cm^{-1} are noted as the ν_1, ν_2 and ν_3 bands, respectively (Macernis et al., 2021; Saito and Tasumi, 1983; Streckaite et al., 2020). The Raman bands of different isomers in the ν_2 region are very different from each other, for there are big differences in peak wavenumber and intensity. For the ν_1 and ν_3 bands, the difference is mainly at the change of full width at half maxima

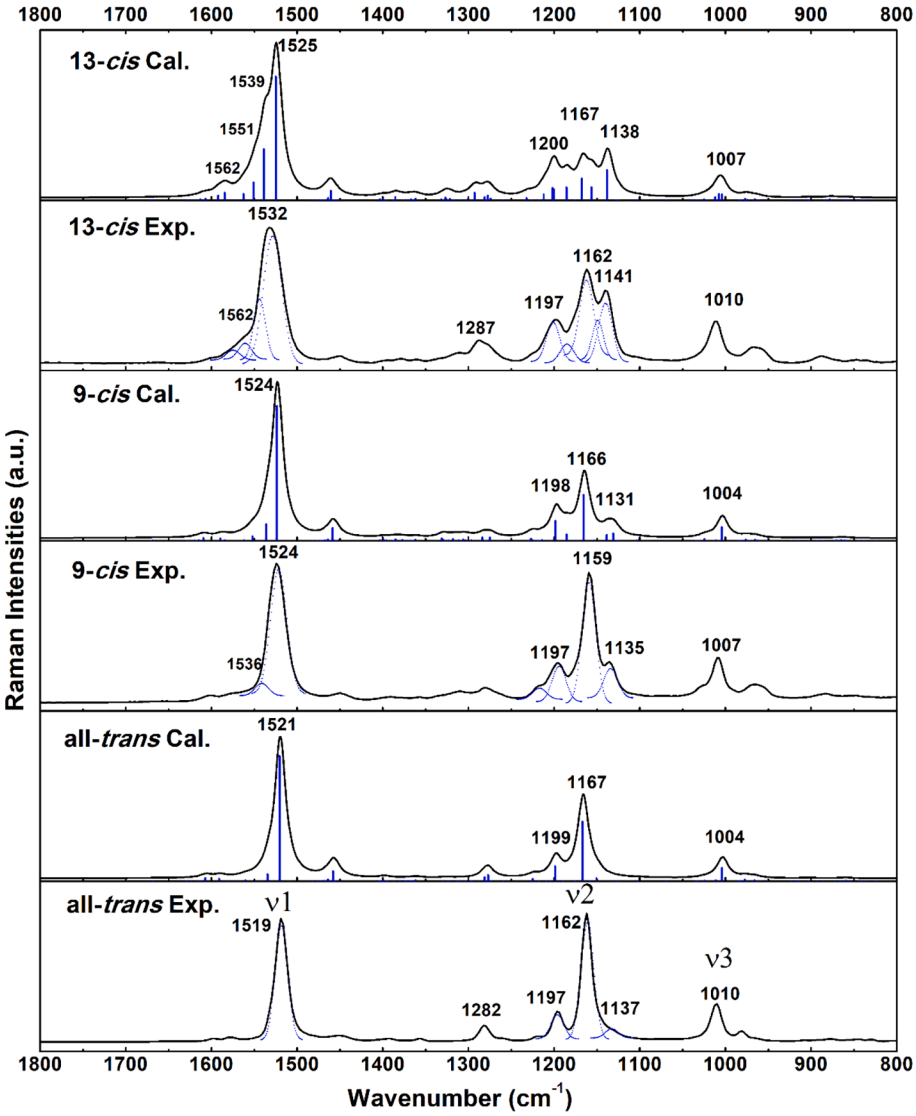

Fig. 2. The experimental (Exp.) and calculated (Cal.) Raman spectra of all-*trans*, 9-*cis* and 13-*cis* isomers of astaxanthin. The doted blue lines in the Exp. spectra are the fitted split peaks. The blue lines in the Cal. spectra are the Raman activity intensities of the molecular vibrational modes. (For interpretation of the references to colour in this figure legend, the reader is referred to the web version of this article.)

intensity (FWHM). The different spectra of these three AST isomers were analyzed by combining experiments with theoretically calculated spectra.

The AST molecule contains 96 atoms, therefore, it has 282 vibrational modes. The calculated Raman activity intensities of vibrations of ten isomers are list in the Tables 1 and 2, and they are also shown in Figs. 2 and 3 in blue lines. The calculated Raman activity intensities can be converted into the Raman intensities by the theoretical formula of Raman scattering using the wavelength of laser in the experiment (Novikov et al., 2022). The calculated Raman activity intensities of 16 vibrational modes of all-*trans* isomer exceeds 10000, and the Raman activity intensities of 237 vibrational modes is less than 1000. As shown in Fig. S1 in Supporting Information, the Raman activity intensities of vibrational modes below 800 cm^{-1} and above 1800 cm^{-1} are very weak. These weak vibrational modes are relatively difficult to be observed on both experimental and calculated Raman spectra. Therefore, only Raman bands in the 800–1800 cm^{-1} range can generally be observed in the experiment. In this work, the vibrational modes of strong Raman bands are assigned corresponding to the experimental spectra. And as shown in Tables 1 and 2, most of the vibrational modes and PEDs of these ten isomers are different. But most of previous work used the vibrational modes of β-carotene to analyze the Raman spectra of different isomers of AST, which seriously affect the correct analysis of astaxanthin Raman spectroscopy, especially in-situ Raman analysis in vivo (Requena et al., 2008; Subramanian et al., 2014).

The Raman spectrum of all-*trans* AST, which is the most common isomer in nature, is firstly discussed. The experimental and calculated Raman spectra are shown in Fig. 2, while the wavenumbers, intensities and assignments of the recognizable Raman bands are shown in Table 1. The structure of all-*trans* AST molecule has Ci symmetry, therefore, the distributions of the vibrational modes are also centrosymmetric. In the 1500–1700 cm^{-1} regions, the bands are mainly from the stretching vibrational modes of carbon–carbon double bonds. In the Fig. 2 and Table 1, the most intense ν_1 band at 1519 cm^{-1} is from the symmetry stretching of carbon-carbon double bonds of the whole polyene chain, the PED of C13 = C14, C13′=C14′ and C15 = C15′ stretching vibrations are above 10 percent, and the PED of C11 = C12, C11′=C12′, C9 = C10 and C9 = C10′ are less than 10 percent. It should be noted that there may be a very weak shoulder peak covered in this strong band, whose simulated wavenumber is 1535 cm^{-1}, comes from the asymmetric stretching of C15 = C15′, C13 = C14 and C13′=C14′. In the 800 to 1500 cm^{-1} regions in Fig. 2, the bands are mainly from the stretching vibration of C—C single bonds, and bending of C—H bonds. In the ν_2 region, the moderate intensity band at 1282 cm^{-1} is mainly from the rocking vibration of C11-H and C11′-H bonds. There is one shoulder band from the bending of C3-O20-H and C3′-O20′-H angles. The weak band at 1218 cm^{-1} is from the stretching of carbon-carbon single bonds of the polyene chain, mainly from C10-C11, C10′-C11′, C12-C13, C12′-C13′ bonds. The strong band at 1197 cm^{-1} mainly is from the stretching of C8-C9, C8′-C9′ bonds. The very strong band at 1162 cm^{-1} is mainly from symmetry stretching of C14-C15, C14′-C15′, C10-C11, C10′-C11′ bonds. There is a weak shoulder band at about 1137 cm^{-1}, which is from asymmetric stretching of C14-C15, C14′-C15′, C10-C11, C10′-C11′ bonds. The strong band at 1010 cm^{-1} is from rocking vibration of methyl groups on the chain, which are $C20H_3$, $C20'H_3$, $C19H_3$, $C19'H_3$.

3.1.2. Interpretation of Raman spectrum of 9-cis isomer

As shown in Fig. 1, for the all-*trans* isomer, the substituent C7 = C8 group and C11 = C12 group are on different side of the C9 = C10 double bond plane. While for the 9-*cis* isomer, the substituent C7 = C8 group and C11 = C12 group are on one side of the C9 = C10 double bond plane. This major structural difference would change the vibrational modes and Raman spectrum of the 9-*cis* isomer. As shown in Table 1, the assignments and PEDs of 9-*cis* isomer are not symmetric, since it is not a symmetric molecule. In the 1500–1700 cm^{-1} regions, the bands are also from the stretching of carbon-carbon double bonds. The most intense ν_1 band at 1524 cm^{-1} is mainly from the stretching of C13′=C14′ and C13 = C14. There is also a shoulder band, which is mainly from str C15 = C15′ and C11′=C12′, its simulated wavenumber is still at 1536 cm^{-1}. But the intensity of this shoulder is a little stronger than that of the all-*trans*, which explains the fact that the ν_1 FWHM observed in the experiment is a little wider than the all-*trans* isomer, and the experimental ν_1 wavenumber of 9-*cis* (1524 cm^{-1}) is higher than all-*trans* isomer (1519 cm^{-1}). The very strong band in the ν_2 region at 1159 cm^{-1} is from the stretching of C14-C15 and C10′-C11′. As shown in the Fig. 2 and Table 1, the most significant difference from all-*trans* isomers is that 9-*cis* has a moderate intensity band at 1135 cm^{-1}. The Raman spectral difference between *cis-trans* isomers can also be found in many carotenoids in previous reports, like β-carotene (Koyama et al., 1982), neurosporene (Koyama et al., 1988), β-Apo-8′- carotenal (Hashimoto et al., 1993), spheroidene (Jiang et al., 1996). Based on this 1135 cm^{-1} Raman band in Fig. 2, these two isomers can be easily distinguished. This band is composed of two overlapping peaks. The vibrational mode of first one (simulated at 1139 cm^{-1}) is mainly from stretching of C14-C15, with part of C6-C7 stretching vibration. The vibrational mode of the second one (simulated at 1131 cm^{-1}) is mainly from stretching of C6-C7, with part of C14-C15 stretching vibration.

3.1.3. Interpretation of Raman spectrum of 13-cis isomer

The 13-*cis* isomer is not a symmetric molecule, therefore the assignments and PEDs are also not symmetric. As shown in Fig. 2, the differences between 13-*cis*, 9-*cis* and all-*trans* isomers are mainly in the 1500–1700 cm^{-1} region and the 1100–1300 cm^{-1} region. The most intense ν_1 band at 1532 cm^{-1} is also mainly from the stretching of C13′=C14′ and C13 = C14 (simulated at 1525 cm^{-1}), but there are also several shoulder peaks. The discernible shoulder band at 1562 cm^{-1} is from the stretching of C5′=C6′ and C5 = C6. The overlapping shoulder band (simulated at 1551 cm^{-1}) is mainly from stretching of C5′=C6′, C5 = C6 and C7 = C8 bonds. The other overlapping strong shoulder band (simulated at 1539 cm^{-1}) is mainly from stretching of C15 = C15′ and C11′=C12′ bonds. One of the possible reasons for this band broadening is the superimposition of several shoulder peaks. Therefore, this band shows a much larger FWHM in the experiment than the all-*trans* isomer (Subramanian et al., 2014). In the 1100–1300 cm^{-1} ν_2 region (Fig. 2), the strong band at 1141 cm^{-1} is from the stretching of C14-C15, C13-C20 and C14′-C15′. Its Raman activity intensity is 133809, while the intensity of 9-*cis* is 63504, and the intensity of all-*trans* is 37477. Therefore, it can be clearly observed in the experimental spectra that the band of 13-*cis* is the strongest, and the intensity of 9-*cis* and all-*trans* gradually decreases. The strong bands at 1162 and 1197 cm^{-1} are actually formed by the superposition of a series of peaks, so the FWHMs are much wider than the all-*trans* isomer. The simulated Raman band shows some difference at the ν_2 region, maybe due to that the simulated 1167 cm^{-1} band is not strong enough.

3.1.4. Interpretation of Raman spectrum of 15-cis isomer

The structures and Raman spectra of other geometric isomers (15-*cis* and di-*cis* isomers) of AST are theoretically studied, whose proportions are usually less than 5% (Yu and Liu, 2020). The theoretical and experimental spectra of the above three isomers (all-*trans*, 9-*cis*, 13-*cis*) are very consistent, so the theoretical simulation spectra of other isomers are also of great reference value. Their optimized structures are shown in Fig. 1, and the geometry parameters are provided in the Tables S2-S4 of supporting information. The 15-*cis* AST molecule has C2 symmetry, therefore, the PEDs of the vibrational modes are symmetric. The calculated Raman spectrum of 15-*cis* is shown in Fig. 3, while the

Table 1
Comparison between the experimental and theoretical calculated Raman spectra of the all-*trans,* 9-*cis* and 13-*cis* isomers of astaxanthin, with the assignments and PED of vibrational modes at B3LYP/6-311 + G(d,p) Level.

all-*trans*						9-*cis*						13-*cis*					
Exp	Int	Cal	Act Int	Δv	Assignments (PED %)	Exp	Int	Cal	Act Int	Δv	Assignments (PED %)	Exp	Int	Cal	Act Int	Δv	Assignments (PED %)
1596	w	1607	40,175	11	νC7 = C8(13), C7′=C8′(13)	1602	w	1609	25,439	7	νC7′=C8′(15), C7 = C8(12)	1599	vw	1592	20,371	−7	νC9 = C10(18), C9′=C10′(15), C15′=C15′(11)
1578	w	1591	32,681	13	νC9 = C10(19), C9′=C10′(19)	1572	w	1589	21,732	17	νC9′=C10′(23), C9 = C10 (13)		sh	1584	34,568		νC11 = C12(14), C5′=C6′(11), C5 = C6(11)
	sh	1535	90,302		ν_{as}C15 = C15′(22), C13 = C14(11), C13′=C14′(11)	1553	vw	1552	39,437	−1	νC5′=C6′(25), C5 = C6(11)	1562	sh	1562	29,529	0	νC5′=C6′(29), C5 = C6 (15)
1519	vs	1521	1,652,378	2	ν_{s}C13 = C14(11), C13′=C14′(11), C15 = C15′(10)		sh	1536	145,503		νC15 = C15′(23), C11′=C12′ (11)		sh	1551	79,306		νC5′=C6′(17), C5 = C6 (15), C7 = C8(12)
1450	w	1458	132,315	8	δC20H_3(16), C20′H_3(16)	1524	vs	1524	1,186,663	0	νC13′=C14′(13), C13 = C14 (12)		sh	1539	225,872		νC15 = C15′(31), C11′=C12′(13)
1394	w	1400	10,398	6	βC3-O20-H(15), C3′-O20′-H(15)	1450	w	1459	112,570	9	δC20H_3(24), C20′H_3(23)	1532	vs	1525	546,162	−7	νC13 = C14(17), C13′=C14′(17)
1356	w	1362	15,255	6	ρC14-H(13), C14′-H(13)		sh	1227	18,973		ρC10-H(15), νC10-C11(10)	1287	m	1293	33,714	6	ρC15-H(21), C12-H(18)
	sh	1281	50,447		βC3-O20-H(10), C3′-O20′-H(10)		sh	1226	13,627		νC1-C2(13), ρC10-H(10)		sh	1232	10,570		ρC14-H(17), νC12-C13 (11), C14-C15(10)
1282	m	1277	80,353	−5	ρC11-H(13), C11′-H(13)	1197	m	1198	174,308	1	νC8′-C9′(12), ρC10′-H(10), C11′-H(10), C14-H(10)		sh	1212	26,280		ρC10-H(16), νC8-C9(10), ρC12-H(10)
1218	w	1225	29,503	7	νC10-C11(11), C10′-C11′(11), C12-C13(10), C12′-C13′(10)		sh	1186	55,456		νC14′-C15′(29), C14-C15 (17), ρC14′-H(10)		sh	1202	55,571		ρC14′-H(14), C12′-H(12), νC8-C9(11)
1197	s	1199	196,296	2	νC8-C9(13), C8′-C9′(13)	1159	vs	1166	405,549	7	νC14-C15(30), C10′-C11′ (18)	1197	s	1200	50,139	3	ρC14-H(15), νC14-C15(10)
1162	vs	1167	785,332	5	ν_{s}C14-C15(15), C14′-C15′(15), C10-C11(13), C10′-C11′(13)		sh	1139	49,113		νC10-C11(22), C6-C7(11)		sh	1186	57,973		νC14′-C15′(28), C10′-C11′ (12)
1137	sh	1151	37,477	14	ν_{as}C14-C15(16), C14′-C15′(16), C10-C11(10), C10′-C11′(10)	1135	m	1131	63,504	−4	νC6-C7(14), C10-C11(13)	1162	s	1167	96,186	5	νC10-C11(43)
1010	s	1004	174,027	−6	ρC20H_3(12), C20′H_3(12), C19H_3(11), C19′H_3(11)	1026	w	1025	13,781	−1	ρC9H_3(17), C13H_3(15), C13′H_3(12), C9′H_3(11)		sh	1156	57,527		νC10′-C11′ (26)
981	m	977	20,507	−4	ω_{s}C8-H(11), C10-H(11), C11-H(11), C8′-H(11), C10′-H(11), C11′-H(11)	1007	s	1004	119,940	−3	ρC20H_3(16), C20′H_3(16), C19H_3(12), C19′H_3(12)	1141	s	1138	133,809	−3	νC14-C15(30), C13-C20 (13), C14′-C15′(10)
965	vw	966	15,020	1	ω_{as}C12-H(14), C12′-H(14), C8-H(12), C8′-H(12)	967	sh	976	11,004	9	ω_{s}C8′-H(18), C10′-H(10)	1010	s	1007	28,982	−3	ρC20H_3(16), C19H_3(14)
906	w	902	3808	−4	ω_{as}C10-H(23), C10′-H(23), C11-H (10), C11′-H(10)	963	m	965	10,038	2	ω_{as}C12′-H(20), C8′-H(17), C11′-H(11), C8-H(10)	967	m	977	6569	10	ωC11′-H(15), C12′-H(14), C8′-H(12)
877	w	859	5233	−18	ω_{as}C7-H(17), C7′-H(17)							959	sh	965	4452	6	ωC12′-H(22), C8′-H(13), C11′-H(13)

Abbreviations: PED, potential energy distribution (PED above 10 percent are listed); Exp, the wavenumber of experimental Raman shift (in cm^{-1}); Cal, the wavenumber of calculated Raman shift (in cm^{-1}); Act Int, the calculated Raman activity intensity is in A^4/AMU; Δv, the calculated Raman shift minus experimental Raman shift of the vibrational mode (in cm^{-1}); vs, very strong; s, strong; m, medium; w, weak; vw, very weak; sh, shoulder peak; β, in plane bending; ρ, rocking; δ, scissoring; ν, stretching; ω, wagging; as, asymmetry; s, symmetry.

Table 2
The calculated Raman spectra with the assignments and PED of vibrational modes of the 15-*cis*, 9,9′-di-*cis*, 9,13-di-*cis*, 9,13′-di-*cis*, 9,15-di-*cis*, 13,13′-di-*cis*, 13,13′-di-*cis* and 13,15-di-*cis* isomers of astaxanthin.

15-*cis*			9,9′-di-*cis*			9,13-di-*cis*			9,13′-di-*cis*			9,15-di-*cis*			13,13′-di-*cis*			13,15-di-*cis*		
Cal	Act Int	Assignments (PED %)	Cal	Act Int	Assignments (PED %)	Cal	Act Int	Assignments (PED %)	Cal	Act Int	Assignments (PED %)	Cal	Act Int	Assignments (PED %)	Cal	Act Int	Assignments (PED %)	Cal	Act Int	Assignments (PED %)
1581	39,295	ν_{as}C5 = C6 (12), C5′=C6′ (12), C13 = C14(10), C13′=C14′ (10)	1611	34,008	ν_{s}C7 = C8 (20), C7′=C8′ (20), C5 = C6 (12), C5′=C6′ (12)	1590	26,222	νC9 = C10 (17), C9′=C10′ (15), C15 = C15′(10)	1564	25,244	νC5 = C6(34), C5′=C6′(23)	1609	21,690	νC7′=C8′(20), C9 = C10(11), C13′=C14′ 10)	1607	34,344	ν_{s}C15 = C15′ (13), C7 = C8 (12), C7′=C8′ (12), C9 = C10 (10), C9′=C10′ (10)	1606	43,223	νC9 = C10 (15), C7 = C8 (12), C7′=C8′ (10)
1550	89,953	ν_{as}C5 = C6 (17), C5′=C6′ (17)	1539	270,263	ν_{s}C15 = C15′ (57)	1555	94,713	νC5 = C6(19), C5′=C6′(14), C7 = C8(10)	1553	41,407	νC5′=C6′(19), C5 = C6(14), C7 = C8(11), C7′=C8′(10)	1583	27,007	νC11′=C12′ (21), C11 = C12(11), C13 = C14(10)	1593	31,028	ν_{s}C9 = C10 (16), C9′=C10′ (16), C15 = C15′(15)	1563	35,702	νC5 = C6(22), C5′=C6′(22)
1529	355,259	ν_{s}C13 = C14 (17), C13′=C14′ (17)	1527	881,409	ν_{s}C13 = C14 (17), C13′=C14′ (17)	1540	298,127	νC15 = C15′ (17), C11′=C11′(16)	1542	331,885	νC15 = C15′ (24), C11′=C12′ (11)	1553	53,627	νC5′=C6′(15), C5 = C6(15), C7′=C8′(11), C7′=C8′(10)	1565	74,549	ν_{s}C5 = C6(22), C5′=C6′(22)	1552	22,936	νC5 = C6(24), C5′=C6′(15)
1521	315,981	ν_{s}C15 = C15′ (32), C11 = C12(10), C11′=C12′ (10)	1459	75,878	δC20H$_3$(30), C20′H$_3$(30)	1527	629,632	νC13 = C14 (16), C13′=C14′(16)	1527	487,748	νC13 = C14 (17), C13′=C14′ (17)	1531	591,110	νC13 = C14 (18), C13′=C14′ (13)	1545	448,847	ν_{s}C15 = C15′ (12), C11 = C12(10), C11′=C12′(10)	1535	1,080,430	νC15 = C15′ (23), C11′=C12′ (15), C13 = C14(10)
1457	30,273	δC20H$_3$(29), C20′H$_3$(29)	1384	32,631	ρC10-H(12), C10′-H(12)	1461	41,703	δC20′H$_3$(37), C20H$_3$(12)	1461	26,432	δC20H$_3$(48)	1524	220,142	νC15 = C15′ (48)	1527	461,411	ν_{s}C13 = C14 (22), C13′=C14′(22)	1380	30,080	δC19H$_3$(29), ρC14-H(22), δC20′H$_3$(13)
1254	111,122	ρC15-H(26), C15′-H(26), νC15 = C15′ (12)	1331	45,130	ρC7-H(19), C7′-H(19)	1292	85,811	ρC12-H(18), C15-H(14)	1382	33,363	ρC10-H(13), δC19′H$_3$(11)	1254	139,119	ρC15-H(32), C15′-H(23)	1465	28,682	δC19H$_3$(21), C19′H$_3$(21), C20H$_3$(11), C20′H$_3$(11)	1311	37,252	ρC12-H(25), C11-H(13)
1206	19,889	ρC10-H(13), C10′-H(13)	1308	41,733	ρC15-H(17), C15′-H(17)	1203	42,030	ρC14-H(15), νC14-C15(12), ρC10′-H(10)	1329	28,142	ρC12′-H(17), C14′-H(13)	1211	23,554	ρC12-H(13), C14-H(11), C10-H(10)	1379	33,255	δ_{s}C19H$_3$(19), C19′H$_3$(19)	1263	103,425	ρC15-H(20), C14-H(17), C15′-H(14)
1201	140,870	ρC10-H(11), C10′-H(11), ν_{s}C8-C9(10), C8′-C9′(10)	1228	33,562	ρC10-H(13), C10′-H(13), ν_{s}C10-C11 (12), C10′-C11′(12)	1202	61,779	ρC12′-H(13), C14′-H(13), νC8′-C9′(12), ρC10′-H(11), C8′-H(10)	1304	29,120	ρC8-H(21), C12-H(19)	1203	132,762	ρC10′-H(14), C12′-H(12), C8′-H(10)	1324	111,608	ν_{s}C15 = C15′ (12), ρC12-H (12), C12′-H (12)	1241	102,967	ρC14′-H(20), C12′-C13′(18)
1165	187,256	ν_{s}C10-C11 (22), C10′-C11′(22)	1200	204,971	ρC12-H(14), C12′-H(14), C14-H(10), C14′-H(10)	1183	99,908	νC14′-C15′(33)	1275	26,022	ρC11′-H(28), C15′-H(11), C15-H(10)	1180	32,052	νC14′-C15′ (18), C14-C15 (15), C10′-C11′(14)	1203	165,886	ρC10-H(13), C10′-H(13), C12-H(10), C12′-H(10)	1204	165,779	ρC10′-H(17), C12′-H(14), C8′-H(11), νC8′-C9′(10)
1055	21,853	ν_{s}C14-C15 (23), C14′-C15′(23), C15 = C15′(11)	1162	237,945	ν_{s}C14-C15 (24), C14′-C15′(24)	1156	79,894	νC10′-C11′ (26), C12′-C13′ (14)	1203	130,997	ρC12-H(12), C14-H(11), C10′-H(10), C12′-H(10)	1159	117,482	νC10′-C11′ (21), C14′-C15′(11), C14-C15(10)	1170	89,956	ν_{s}C10-C11(27), C10′-C11′(27)	1174	52,548	νC10′-C11′ (25), C14′-C15′(11)
1003	47,278	ρC20H$_3$(12), C20′H$_3$(12), C19H$_3$(11), C19′H$_3$(11)	1138	44,808	ν_{s}C6-C7(12), C6′-C7′(12), C10-C11(10), C10′-C11′(10)	1138	97,042	νC14-C15(24), C6-C7(15)	1167	74,203	νC10′-C11′ (32)	1141	50,375	νC10-C11 (29), C6-C7 (10), C8 = C9 (10)	1129	39,175	ν_{s}C6-C7(12), C6′-C7′(12), C1-C6(10), C1′-C6′(10)	1170	92,479	νC10-C11(44)

(*continued on next page*)

Table 2 (*continued*)

15-*cis*			9,9′-di-*cis*			9,13-di-*cis*			9,13′-di-*cis*			9,15-di-*cis*			13,13′-di-*cis*			13,15-di-*cis*		
Cal	Act Int	Assignments (PED %)	Cal	Act Int	Assignments (PED %)	Cal	Act Int	Assignments (PED %)	Cal	Act Int	Assignments (PED %)	Cal	Act Int	Assignments (PED %)	Cal	Act Int	Assignments (PED %)	Cal	Act Int	Assignments (PED %)
			1130	126,336	ν_sC10-C11 (13), C10′-C11′(13), C6-C7(11), C6′-C7′(11)	1130	110,590	νC6-C7(20), C14-C15(13)	1141	179,690	νC13′-C14′ (24), C10-C11 (18)	1132	36,225	νC6-C7(15), ρC16H$_3$(11), C17H$_3$(10)	1127	111,196	ν_sC2-C3(13), C2′-C3′(12), C14-C15(10), C14′-C15′(10)	1149	74,494	νC14-C15 (18), C14′-C15′(13), C10′-C11′(10)
			1005	91,115	ρC20H$_3$(14), C20′H$_3$(14), C19H$_3$(12), C19′H$_3$(12)	1008	39,377	ρC20H$_3$(24), C19H$_3$(20)	1137	38,398	νC14′-C15′ (15), C14-C15 (14), C6-C7 (11)	1004	53,335	ρC20H$_3$(16), C20′H$_3$(16), C19′H$_3$(14), C19H$_3$(13)	1125	114,481	ν_sC14-C15(17), C14′-C15′(17), C3-O21(10), C3′-O21′(10)	1060	70,049	ρC20H$_3$(15), νC14′-C15′ (12), C14-C15 (10)
						1004	25,069	ρC20′H$_3$(24), C19′H$_3$(10)	1008	32,038	ρC20′H$_3$(17), C19′H$_3$(12), C16′H$_3$(10), C17′H$_3$(10)				1013	28,556	ρC20H$_3$(14), C20′H$_3$(14), C19H$_3$(12), C19′H$_3$(12)	1002	27,769	ρC20H$_3$(26), C20′H$_3$(14), C19′H$_3$(11)
						1590	26,222	νC9 = C10 (17), C9′=C10′ (15), C15 = C15′(10)							1009	27,512	ρC19H$_3$(12), C19′H$_3$(12), C16H$_3$(10), C16′H$_3$(10), C17H$_3$(10), C17′H$_3$(10)			

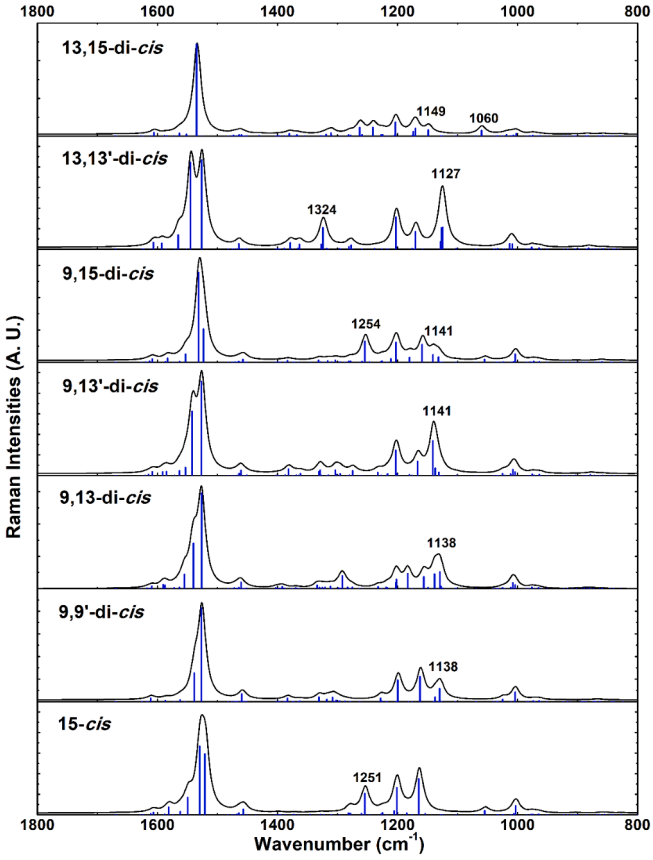

Fig. 3. The calculated Raman spectra of 15-*cis* and di-*cis* isomers of astaxanthin. The blue lines are the Raman activity intensities of the molecular vibrational modes. (For interpretation of the references to colour in this figure legend, the reader is referred to the web version of this article.)

assignments and PEDs of strong bands are listed in Table 2. Unlike all-*trans*, 9-*cis* and 13-*cis*, the15-*cis* isomer has a strong characteristic Raman band at 1251 cm^{-1} in the ν_2 region, which comes from rocking vibration of C15-H, C15′-H and stretching of C15 = C15′. The strong intensity of this band may be caused by the *cis* symmetry of C15 = C15′ group. This fact of characteristic Raman bands of the isomers having the *cis* form around the C15 = C15′ bond was also reported in the β-carotene (Saito and Tasumi, 1983). As shown in Fig. 3, similar to the all-*trans* isomer, the15-*cis* isomer does not have an observable band in the range of 1135 to 1140 cm^{-1}.

3.1.5. *Interpretation of Raman spectra of six di-cis isomers*

There are 6 di-*cis* isomers of AST, they are 9,9′-di-*cis*, 9,13-di-*cis*, 9,13′-di-*cis*, 9,15-di-*cis*, 13,13′-di-*cis*, 13,15-di-*cis* isomers. It can be seen from Fig. 3 that the simulated spectra of the 6 *cis-trans* isomers also have some different characteristics bands. Their spectra have the following distinguishable features: 1) In Fig. 3, the Raman spectrum of 9,9′-di-*cis* is similar to 9-*cis* except the 1130 cm^{-1} band. This band of 9-*cis* (Fig. 2) is consisted by two peaks mainly from stretching of C6-C7 and C10-C11 stretching vibration. While this band of 9,9′-di-*cis* is consisted by two peaks from the stretching of both C6-C7, C10-C11 and C6′-C7′, C10′-C11′ stretching vibration, since 9,9′-di-*cis* has Ci symmetry. This cause that the intensity of this band of 9,9′-di-*cis* is about twice of 9-*cis*, and this difference is very consistent with the experimental spectrum (Subramanian et al., 2014). 2) The Raman spectrum of 9,13-di-*cis* has two band near to 1200 cm^{-1}, while other isomers have only one band. 3) In Fig. 3, the spectrum of 9,13′-di-*cis* is similar to 9,13-di-*cis*. But the intensity of 1141 cm^{-1} band of 9,13′-di-*cis* is higher than 9,13-di-*cis*. 4) The Raman spectrum of 9,15-di-*cis* has a strong band at 1254 cm^{-1},

which is from the rocking vibration of C15-H and C15′-H. 5) The Raman spectrum of 13,13′-di-*cis* has a strong band at 1324 cm^{-1}, which is from stretching of C15 = C15′, and the rocking vibration of C12-H and C12′-H. 6) In Fig. 3, the Raman spectrum of 13,15-di-*cis* has a medium intensity band near to the ν_3 band at 1060 cm^{-1}, which is from rocking mode of C20 from CH_3 group, and the stretching of C14′-C15′ and C14-C15. And the 13,15-di-*cis* isomer does not have an observable band at about 1135 to 1140 cm^{-1}. This characteristic Raman difference around 1130 cm^{-1} bands in the ν_2 region has also been found and used to distinguish *cis-trans* isomers of many carotenoids, for instance, in β-carotene (Koyama et al., 1982), neurosporene (Koyama et al., 1988), β-Apo-8′- carotenal (Hashimoto et al., 1993), spheroidene (Jiang et al., 1996), and etc. The assignment of this important band is specially listed in Table 3.

Therefore, when the experimental Raman spectrum of an unknown pure AST isomer is measured, the calculated spectra of ten isomers can help to the identification of the structure of this AST isomer. In principle, these characteristic bands could also be useful for Raman recognition of AST in a biological system. For example, Raman spectroscopy may be used for in situ recognition and conversion mechanism of AST isomers in different living organism, and it may also be used for the study of the different stability of AST isomer in soybean and sunflower oils. Of course, much more work needs to be done for practical applications in the complex biological system.

3.2. Discussion of Raman spectra and structure of AST cis–trans isomers.

Many early works considered that the strong Raman intensity of the polyenic or carotenoid pigment was due to resonance Raman effect (Bergamonti et al., 2011; Meinhardt-Wollweber et al., 2018). However, our data in this work seem not support this assumption. There are several evidence to prove our viewpoint in this work. Firstly, the 785 nm laser used in this work is far away from the AST 460 nm absorption band. But still, the Raman signals are very strong with 785 nm laser, and the spectrum is similar to the spectrum measured by 532 nm laser (Shao et al., 2019; Sharma et al., 2015). Secondly, for the simulation of Raman activity intensity in this present quantum chemistry calculations, the laser excitation was not taken into account. As can be seen from Tables 1 and 2 that the Raman activity intensities of many vibrational modes are extremely strong, even reaching the order of millions, while the Raman activity intensity of most common molecules is only in the range of one hundred. Therefore, this strong Raman intensity of the experiment mainly come from its own strong Raman activity, not the resonance effect. Thirdly, as shown in Fig. 2, the simulated normal Raman spectrum (without resonance effect) is quite consistent with the experimental result, also confirming that it is not a resonance Raman effect.

Table 3
Raman bands used to distinguish AST *cis-trans* isomers.

Isomer	Exp	Int	Cal	Act Int	Assignments (PED %)
all-*trans*	1137	sh	1151	37,477	ν_{as}C14-C15(16), C14′-C15′(16), C10-C11(10), C10′-C11′(10)
9-*cis*	1135	m	1131	63,504	νC6-C7(14), C10-C11(13)
13-*cis*	1141	s	1138	133,809	νC14-C15(30), C13-C20(13), C14′-C15′(10)
15-*cis*			–	–	–
9,9′-di-*cis*			1138	44,808	ν_sC6-C7(12), C6′-C7′(12), C10-C11(10), C10′-C11′(10)
9,13-di-*cis*			1138	97,042	νC14-C15(24), C6-C7(15)
9,13′-di-*cis*			1141	179,690	νC13′-C14′(24), C10-C11(18)
9,15-di-*cis*			1141	50,375	νC10-C11(29), C6-C7(10), C8 = C9(10)
13,13′-di-*cis*			1127	111,196	ν_sC2-C3(13), C2′-C3′(12), C14-C15(10), C14′-C15′(10)
13,15-di-*cis*			1149	74,494	ν C14-C15(18), C14′-C15′(13), C10′-C11′(10)

As shown in Fig. 1, all-*trans*- AST can be isomerized in to mono-*cis* forms, like 9-*cis*, 13-*cis*, 15-*cis*, and 6 kinds of di-*cis* isomers, like 9,9′-di-*cis*, 9,13-di-*cis*, 9, 13′-di-*cis*, 9,15-di-*cis*, 13,13′-di-*cis*, 13, 15-di-*cis*. In the statistics of previous review work on organisms, different aquatic organisms have different proportion of AST isomers, and the all-*trans* isomer accounts for the main proportion (Yu and Liu, 2020). For instance, the flesh of rainbow trout, salmon, arctic charr and halibut contains about 75% to 100% all-*trans* AST; the flesh of cod, sprat, herring contain about 50% to 65% all-*trans* AST; the flesh of crustacean organisms, such as krill, shrimp, white prawn, contains about 60% to 90% all-*trans* AST (Yu and Liu, 2020). While 9-*cis* and 13-*cis* are the other isomers with the largest proportion, sometimes reaching more than 10%. 15-*cis* is usually less than 3%, and the content of di-*cis* is even lower. Therefore, in this work, we mainly focused on all-*trans*, 9-*cis* and 13-*cis* these three kinds of geometric isomers from experiments and calculations, and other geometric isomers are analyzed by theoretical calculations.

The single-point energies of these ten isomers are all calculated. The energy of all-*trans* isomer is the lowest, and the energy differences of the other isomers relative to the all-*trans* isomer are listed in Table 4. Based on the Maxwell-Boltzmann distribution, the ratios of different isomers are estimated through their relative energies. The ratio of all-*trans* configuration is approximately 70%, 9-*cis* and 13-*cis* are about 10%, the other isomers are less than 2%. The total content of di-isomers does not exceed 10%. The 15-*cis* is the least among mono-*cis* isomers, while 9,15-di-*cis* and 13, 15-di-*cis* are the least among di-*cis* isomers. The calculated ratios are well consistent with the previously reported ratios of isomers in natural organisms or chemical conditions (Euglert and Vecchi, 1980; Holtin et al., 2009; Yu and Liu, 2020). Therefore, based on Boltzmann distribution calculated from the energies of isomers, it can be reasonably explained why the isomers have these different proportions.

The experimental crystal structure of all-*trans* isomer of AST was obtained through X-ray diffraction (Bartalucci et al., 2007). The calculated structure parameters of this work are compared with the experiment, involving the bond lengths, angles and dihedral angles in Table S1. Since the all-*trans* AST molecule has Ci symmetry, the structural parameters are also symmetric. For instance, the bond lengths of C1-C2 and C1′-C2′ bonds are the same. In the all-*trans* molecule, C6 to C15 with C6′ to C15′ constitute a linear conjugated chain of 40 carbon atoms. The dihedral angle in the chain, like C7-C8-C9-C10 and C14-C15-C15′-C14′, are all near to 180°, and this conjugated chain is nearly flat. The C5-C6, C7-C8, C9-C10, C11-C12, C13-C14 and C15-C15′ bonds are carbon-carbon double bonds, their bond lengths are shorter than 1.4 Å. The C8-C9, C10-C11, C12-C13 and C14-C15 bonds are single bonds in

Table 4
The relative energies and the estimated ratios of astaxanthin geometrical isomers.

AST isomer	ΔEi (kcal/mol)	isomer ratio (%) [a]
all-*trans*	0.000	70.78
9-*cis*	1.111	10.86
13-*cis*	1.182	9.63
15-*cis*	2.462	1.11
9,9′-di-*cis*	2.146	1.89
9,13-di-*cis*	2.171	1.81
9,13′-di-*cis*	2.176	1.80
9,15-di-*cis*	3.424	0.22
13,13′-di-*cis*	2.201	1.72
13,15-di-*cis*	3.538	0.18

[a] The distribution ratios of different isomers are estimated through the Maxwell-Boltzmann distribution.$Ratio = \frac{Ni}{N} = \frac{e^{-Ei/kT}}{\sum_i e^{-Ei/kT}}$, k is Boltzmann constant, T is set as 298.15 K, Ei is the energy of ith isomer, Ni is the molecule number of ith isomer, N is the total molecule number of the isomers (Liu et al., 2011).

conjugated system, their bond lengths are about 1.45 Å. They are shorter than the traditional carbon-carbon single bond, for example, the bond length of C1-C16 exceeds 1.5 Å.

The molecular geometry structures of these ten isomers are all optimized. Their structural parameters like bond lengths, angles and dihedral angles are listed in the Tables S2-S4 of supporting information, respectively. It can be seen from Tables S2 and S3 that the bond lengths and angles of different isomers are very close. The differences in structural parameters between ten isomers mainly lie in the dihedral angles where *cis-trans* isomerism occurs, as shown in Table S4. For instance, the C8-C9-C10-C11 dihedral angles of 9-*cis*, 9,9′-di-*cis*, 9,13-di-*cis*, 9,13′-di-*cis*, 9,15-di-*cis* isomers are near to 0°, while the C8-C9-C10-C11 of other isomers are near to 180°. The C12-C13-C14-C15 dihedral angles of 13-*cis*, 9,13-di-*cis*, 13,13′-di-*cis*, 13,15-di-*cis* isomers are near to 0°, while the C12-C13-C14-C15 of other isomer are near to 180°. These structural parameters may greatly promote in-depth study of the physiological properties of different AST isomers, such as the analysis of their interactions with proteins.

4. Conclusion

In this work, the structures and Raman spectra of all geometric isomers of astaxanthin have been systematically explored. The energies, structure, and Raman spectra of these 10 isomers are obtained based on DFT calculations. From the relative energy of isomers, it can be reasonably explained why the isomers have these different proportions in the nature or chemical synthesis. The vibrational modes and PEDs of these isomers are analyzed. Structural parameters such as bond length, bond angle and dihedral angle of all isomers are also obtained. The Raman spectra simulated by DFT are in good agreement with the available experimental data, explaining well the experimental spectra in terms of Raman shift, intensity change and peak broadening. Moreover, we demonstrate that the different AST isomers have characteristic Raman bands in the 1000 to 1350 cm^{-1}. Therefore, by combining DFT and Raman spectroscopy, all the known geometric isomers of astaxanthin can be well distinguished. The research of molecular vibrational modes and molecular structures have important significance for the in-depth understanding of the chemical and biological properties of AST, and may promote the development of the research on food, nutrition, medicine and other fields in food molecular science.

CRediT authorship contribution statement

Guohua Yao: Methodology, Software, Data curation, Investigation, Writing – original draft. **Muhammad Muhammad:** Methodology, Data curation. **Jiajiang Zhao:** Resources. **Jianguo Liu:** Resources. **Qing Huang:** Conceptualization, Supervision, Project administration, Investigation, Writing – review & editing.

Declaration of Competing Interest

The authors declare that they have no known competing financial interests or personal relationships that could have appeared to influence the work reported in this paper.

Acknowledgements

This work was supported by the National Natural Science Foundation of China (Grants: 11635013, 11775272, 21904127 and 11475217) and the Anhui Provincial Natural Science Foundation (1908085MB53) and Laboratory for Marine Biology and Biotechnology, Qingdao National Laboratory for Marine Science and Technology (MS2019NO01).

Appendix A. Supplementary data

Supplementary data to this article can be found online at https://doi.org/10.1016/j.fochms.2022.100103.

Reference

Ambati, R. R., Phang, S. M., Ravi, S., & Aswathanarayana, R. G. (2014). Astaxanthin: Sources, extraction, stability, biological activities and its commercial applications–a review. *Mar Drugs, 12*, 128–152.

Bartalucci, G., Coppin, J., Fisher, S., Hall, G., Helliwell, J. R., Helliwell, M., et al. (2007). Unravelling the chemical basis of the bathochromic shift in the lobster carapace; new crystal structures of unbound astaxanthin, canthaxanthin and zeaxanthin. *Acta Crystallographica Section B, 63*, 328–337.

Bergamonti, L., Bersani, D., Csermely, D., & Lottici, P. P. (2011). The Nature of the Pigments in Corals and Pearls: A Contribution from Raman Spectroscopy. *Spectrosc Lett, 44*, 453–458.

Buchwald, M., & Jencks, W. P. (1968). Optical properties of astaxanthin solutions and aggregates. *Biochemistry, 7*, 834–843.

de Bruijn, W. J. C., Weesepoel, Y., Vincken, J.-P., & Gruppen, H. (2016). Fatty acids attached to all-trans-astaxanthin alter its cis–trans equilibrium, and consequently its stability, upon light-accelerated autoxidation. *Food Chem, 194*, 1108–1115.

Dennington, R., Keith, T., & Millam, J. (2009). *GaussView 5*. Shawnee Mission, KS: Semichem Inc.

Euglert, G., & Vecchi, M. (1980). trans/cis Isomerization of Astaxanthin Diacetate/Isolation by HPLC. and Identification by 1H-NMR. Spectroscopy of Three Mono-cis- and Six Di-cis-Isomers. *Helv Chim Acta, 63*, 1711–1718.

Frisch, M. J., Trucks, G. W., Schlegel, H. B., Scuseria, G. E., Robb, M. A., Cheeseman, J. R., et al. (2009). *Gaussian 09, D. 01*. Wallingford CT: Gaussian, Inc.

Gong, F., Zhang, C., Zhang, L., & Liu, J. (2020). Changes of carotenoids contents and analysis of astaxanthin geometrical isomerization in Haematococcus pluvialis under outdoor high light conditions. *Aquaculture Research, 51*, 770–778.

Hashimoto, H., Miki, Y., Kuki, M., Shimamura, T., Utsumi, H., & Koyama, Y. (1993). Isolation by high-pressure liquid chromatography of the cis-trans isomers of.beta.-apo-8'-carotenal. Determination of their S0-state configurations by NMR spectroscopy and prediction of their S1- and T1-state configurations by transient Raman spectroscopy. *Journal of the American Chemical Society, 115*, 9216–9225.

Holtin, K., Kuehnle, M., Rehbein, J., Schuler, P., Nicholson, G., & Albert, K. (2009). Determination of astaxanthin and astaxanthin esters in the microalgae Haematococcus pluvialis by LC-(APCI)MS and characterization of predominant carotenoid isomers by NMR spectroscopy. *Analytical and Bioanalytical Chemistry, 395*, 1613–1622.

Honda, M., Kageyama, H., Hibino, T., Osawa, Y., Kawashima, Y., Hirasawa, K., et al. (2021a). Evaluation and improvement of storage stability of astaxanthin isomers in oils and fats. *Food Chem, 352*, 129371–129380.

Honda, M., Murakami, K., Osawa, Y., Kawashima, Y., Hirasawa, K., & Kuroda, I. (2021b). Z-Isomers of Astaxanthin Exhibit Greater Bioavailability and Tissue Accumulation Efficiency than the All-E-Isomer. *Journal of Agricultural and Food Chemistry, 69*, 3489–3495.

Huang, W. E., Li, M., Jarvis, R. M., Goodacre, R., & Banwart, S. A. (2010). Shining light on the microbial world the application of Raman microspectroscopy. *Adv Appl Microbiol, 70*, 153–186.

Jamróz, M. H. (2013). Vibrational Energy Distribution Analysis (VEDA): Scopes and limitations. *Spectrochimica Acta Part A: Molecular and Biomolecular Spectroscopy, 114*, 220–230.

Jiang, Y.-S., Kurimoto, Y., Shimamura, T., Ko-Chi, N., Ohashi, N., Mukai, Y., et al. (1996). Isolation by high-pressure liquid chromatography, configurational determination by 1H-NMR, and analyses of electronic absorption and raman spectra of isomeric spheroidene. *Biospectroscopy, 2*, 47–58.

Kaczor, A., & Baranska, M. (2011). Structural Changes of Carotenoid Astaxanthin in a Single Algal Cell Monitored in Situ by Raman Spectroscopy. *Anal Chem, 83*, 7763–7770.

Kaczor, A., Turnau, K., & Baranska, M. (2011). In situ Raman imaging of astaxanthin in a single microalgal cell. *Analyst, 136*, 1109–1112.

Koyama, Y., Kanaji, M., & Shimamura, T. (1988). CONFIGURATIONS OF NEUROSPORENE ISOMERS ISOLATED FROM THE REACTION CENTER AND THE LIGHT-HARVESTING COMPLEX OF Rhodobacter spheroides G1C. A RESONANCE RAMAN, ELECTRONIC ABSORPTION, AND 1H-NMR STUDY. *Photochemistry and Photobiology, 48*, 107–114.

Koyama, Y., Kito, M., Takii, T., Saiki, K., Tsukida, K., & Yamashita, J. (1982). Configuration of the carotenoid in the reaction centers of photosynthetic bacteria. Comparison of the resonance Raman spectrum of the reaction center of Rhodopseudomonas sphaeroides G1C with those of cis-trans isomers of β-carotene. *Biochim Biophys Acta, 680*, 109–118.

Laury, M. L., Carlson, M. J., & Wilson, A. K. (2012). Vibrational frequency scale factors for density functional theory and the polarization consistent basis sets. *J Comput Chem, 33*, 2380–2387.

Liu, J., & Huang, Q. (2016). Screening of Astaxanthin-Hyperproducing Haematococcus pluvialis Using Fourier Transform Infrared (FT-IR) and Raman Microspectroscopy. *Appl Spectrosc, 70*, 1639–1648.

Liu, P.-W., Zhao, K., & Han, G.-C. (2011). Effects of isomerism on two-photon absorption of substituted benzenes with two pairs of donor–acceptors. *Chem Phys Lett, 514*, 226–233.
Liu, X., Luo, Q., Cao, Y., Goulette, T., Liu, X., & Xiao, H. (2016). Mechanism of Different Stereoisomeric Astaxanthin in Resistance to Oxidative Stress in Caenorhabditis elegans. *J Food Sci, 81*, H2280–H2287.
Liu, X., & Osawa, T. (2007). Cis astaxanthin and especially 9-cis astaxanthin exhibits a higher antioxidant activity in vitro compared to the all-trans isomer. *Biochem Biophys Res Commun, 357*, 187–193.
Macernis, M., Bockuviene, A., Gruskiene, R., Krivorotova, T., & Sereikaite, J. (2021). Raman study for β-ring positioning in β-Carotene complexes with Cyclodextrins and Chitooligosaccharides. *J Mol Struct, 1226*, 129362–129369.
Macernis, M., Sulskus, J., Duffy, C. D. P., Ruban, A. V., & Valkunas, L. (2012). Electronic Spectra of Structurally Deformed Lutein. *The Journal of Physical Chemistry A, 116*, 9843–9853.
Macernis, M., Sulskus, J., Malickaja, S., Robert, B., & Valkunas, L. (2014). Resonance Raman Spectra and Electronic Transitions in Carotenoids: A Density Functional Theory Study. *The Journal of Physical Chemistry A, 118*, 1817–1825.
Meinhardt-Wollweber, M., Suhr, C., Kniggendorf, A.-K., & Roth, B. (2018). Absorption and resonance Raman characteristics of β-carotene in water-ethanol mixtures, emulsion and hydrogel. *AIP Advances, 8*, 055320–055332.
Novikov, V. S., Kuzmin, V. V., Darvin, M. E., Lademann, J., Sagitova, E. A., Prokhorov, K. A., et al. (2022). Relations between the Raman spectra and molecular structure of selected carotenoids: DFT study of α-carotene, β-carotene, γ-carotene and lycopene. *Spectrochimica Acta Part A: Molecular and Biomolecular Spectroscopy, 270*, 120755–120764.
Osterlie, M., Bjerkeng, B., & Liaaen-Jensen, S. (1999). Accumulation of astaxanthin all-E, 9Z and 13Z geometrical isomers and 3 and 3' RS optical isomers in rainbow trout (Oncorhynchus mykiss) is selective. *J Nutr, 129*, 391–398.
Perdew, J. P., Burke, K., & Ernzerhof, M. (1996). Generalized gradient approximation made simple. *Phys Rev Lett, 77*, 3865–3868.
Requena, A., Cerón-Carrasco, J. P., Bastida, A., Zúñiga, J., & Miguel, B. (2008). A Density Functional Theory Study of the Structure and Vibrational Spectra of β-Carotene, Capsanthin, and Capsorubin. *The Journal of Physical Chemistry A, 112*, 4815–4825.
Saito, S., & Tasumi, M. (1983). Normal-coordinate analysis of β-carotene isomers and assignments of the Raman and infrared bands. *J Raman Spectrosc, 14*, 310–321.
Shao, Y., Gu, W., Jiang, L., Zhu, Y., & Gong, A. (2019). Study on the Visualization of Pigment in Haematococcus pluvialis by Raman Spectroscopy Technique. *Sci Rep, 9*, 12097–12105.
Sharma, S. K., Nelson, D. R., Abdrabu, R., Khraiwesh, B., Jijakli, K., Arnoux, M., et al. (2015). An integrative Raman microscopy-based workflow for rapid in situ analysis of microalgal lipid bodies. *Biotechnol Biofuels, 8*, 164–177.
Streckaite, S., Macernis, M., Li, F., Kuthanová Trsková, E., Litvin, R., Yang, C., et al. (2020). Modeling Dynamic Conformations of Organic Molecules: Alkyne Carotenoids in Solution. *The Journal of Physical Chemistry A, 124*, 2792–2801.
Su, F., Yu, W., & Liu, J. (2020). Comparison of effect of dietary supplementation with Haematococcus pluvialis powder and synthetic astaxanthin on carotenoid composition, concentration, esterification degree and astaxanthin isomers in ovaries, hepatopancreas, carapace, epithelium of adult female Chinese mitten crab (Eriocheir sinensis). *Aquaculture, 523*, 735146–735152.
Subramanian, B., Tchoukanova, N., Djaoued, Y., Pelletier, C., Ferron, M., & Robichaud, J. (2014). Investigations on the geometrical isomers of astaxanthin: Raman spectroscopy of conjugated polyene chain with electronic and mechanical confinement. *J Raman Spectrosc, 45*, 299–304.
Visioli, F., & Artaria, C. (2017). Astaxanthin in cardiovascular health and disease: Mechanisms of action, therapeutic merits, and knowledge gaps. *Food & Function, 8*, 39–63.
Yang, C., Hassan, Y. I., Liu, R., Zhang, H., Chen, Y., Zhang, L., et al. (2019). Anti-Inflammatory Effects of Different Astaxanthin Isomers and the Roles of Lipid Transporters in the Cellular Transport of Astaxanthin Isomers in Caco-2 Cell Monolayers. *Journal of Agricultural and Food Chemistry, 67*, 6222–6231.
Yang, C., Zhang, H., Liu, R., Zhu, H., Zhang, L., & Tsao, R. (2017). Bioaccessibility, Cellular Uptake, and Transport of Astaxanthin Isomers and their Antioxidative Effects in Human Intestinal Epithelial Caco-2 Cells. *Journal of Agricultural and Food Chemistry, 65*, 10223–10232.
Yang, L., Qiao, X., Liu, J., Wu, L., Cao, Y., Xu, J., et al. (2021). Preparation, characterization and antioxidant activity of astaxanthin esters with different molecular structures. *Journal of the Science of Food and Agriculture, 101*, 2576–2583.
Yu, W., Zhang, M., Wang, B., Xu, R., Pang, T., & Liu, J. (2021). Dietary Haematococcus pluvialis powder supplementation affect carotenoid content, astaxanthin isomer, antioxidant capacity and immune-related gene expression in Pacific white shrimp, Litopenaeus vannamei. *Aquaculture Research, 52*, 2403–2414.
Yu, W. J., & Liu, J. G. (2020). Astaxanthin isomers: Selective distribution and isomerization in aquatic animals. *Aquaculture, 520*, 734915–734926.
Yuan, J. P., & Chen, F. (1999). Isomerization of trans-astaxanthin to cis-isomers in organic solvents. *J Agric Food Chem, 47*, 3656–3660.
Zajac, G., Machalska, E., Kaczor, A., Kessler, J., Bouř, P., & Baranska, M. (2018). Structure of supramolecular astaxanthin aggregates revealed by molecular dynamics and electronic circular dichroism spectroscopy. *Phys Chem Chem Phys, 20*, 18038–18046.
Zhao, L., Chen, F., Zhao, G., Wang, Z., Liao, X., & Hu, X. (2005). Isomerization of trans-astaxanthin induced by copper(II) ion in ethanol. *J Agric Food Chem, 53*, 9620–9623.